From Images to Interactions: High-Resolution Phase Imaging in Tapping-Mode Atomic Force Microscopy

Martin Stark,* Clemens Möller,†‡§ Daniel J. Müller,†§ and Reinhard Guckenberger*
*Max Planck Institute for Biochemistry, Department of Molecular Structural Biology, D-82152 Martinsried, Germany; †M.E. Müller Institute for Structural Biology, Biozentrum, CH-4056 Basel, Switzerland; ‡Forschungszentrum Jülich, IBI-2, Structural Biology, D-52425 Jülich, Germany; and §Max Planck Institute of Molecular Cell Biology and Genetics, D-01307 Dresden, Germany

ABSTRACT In tapping-mode atomic force microscopy, the phase shift between excitation and response of the cantilever is used as a material-dependent signal complementary to topography. The localization of information in the phase signal is demonstrated with 1.4-nm lateral resolution on purple membrane of *Halobacterium salinarum* in buffer solution. In a first-order approximation, the phase signal is found to correlate with modulations of the tip oscillation amplitude, induced by topography. Extending the analysis to contributions of the tip-sample interaction area as a second-order approximation, a method is proposed to extract information about the interaction from the phase signal for surfaces with a roughness in the order of the tip radius.

INTRODUCTION

Atomic force microscopy (AFM) (Binnig et al., 1986) is capable of imaging biological systems as functional entities in buffer solution and at ambient temperature. Its intriguing signal-to-noise ratio allows single proteins to be directly observed and functionally characterized (Drake et al., 1989; Hoh et al., 1993; Yang et al., 1994; Schabert et al., 1995; Müller et al., 1995; Malkin et al., 1997; Kuznetsov et al., 1997; Czajkowsky and Shao, 1998; Yip et al., 1998; Vinckier et al., 1998; Grandbois et al., 1998; McMaster et al., 1999; Müller and Engel, 1999; Oesterhelt et al., 2000). A complex variety of interactions bound to well-defined structures determines the functionality of biological macromolecules. For a more detailed insight into biological function and processes, methods have to be developed that assist in distinguishing between these interactions and relate them to the structure.

Along with the ability to resolve surface morphology of proteins, the tip-sample interaction in AFM can serve as a model system to assess interaction schemes relevant for the functional behavior of proteins. Thus, it is tempting to question whether the ability of AFM to reveal structure and simultaneously map surface properties can be applied to well-defined molecular structures such as those represented by macromolecules.

In tapping-mode (TM)-AFM (Zhong et al., 1993; Putman et al., 1994; Hansma et al., 1994), the cantilever is excited to oscillate close to its resonant frequency. The AFM tip is only in intermittent contact with the sample surface. Thus, compared with contact-mode AFM, tip-sample interaction times (Tamayo and García, 1996; Sarid et al., 1996; Hillenbrand et al., 2000), and with it lateral forces, are reduced. Changes of the effective (vertical) forces acting on the tip alter the oscillation in amplitude and phase. Recently, it was demonstrated that substructures of single proteins could be revealed by TM-AFM (Dorn et al., 1999; Möller et al., 1999; Viani et al., 2000).

Simultaneously recording the topography and the phase shift of the cantilever oscillation relative to the driving signal as reference allows mapping of interaction properties of a heterogeneous sample. This phase imaging has been applied to explore various material properties, e.g., adhesion and viscoelastic properties (Winkler et al., 1996; Tamayo and García, 1997; Magonov et al., 1997; Noy et al., 1998; Thomann et al., 1998; Chen et al., 1998; San Paulo and García, 2000), capillary forces and wetting (Van Noort et al., 1997; Gil et al., 2000), and even detection of surface charges (Czajkowsky et al., 1998). As recently shown, the phase shift is related to energy dissipated in the tip-sample contact (Cleveland et al., 1998; García et al., 1999; Anczykowski et al., 1999).

Even though various concepts on TM-AFM in general have been published (Anczykowski et al., 1996; Burnham et al., 1997; Whangbo et al., 1998; Bielefeldt and Giessibl, 1999; Behrend et al., 1999; García and San Paulo, 2000; Dürig, 2000; Stark and Heckl, 2000; Stark et al., 2000), the interpretation of phase images remains difficult. The different channels that contribute to the dissipation are not readily accessible, and are strongly influenced by the sample topography.

In this work, we investigate contrast formation in phase imaging under the focus of structure and interaction of a macromolecular system. Based on theoretical considerations, a concept is suggested to decompose the phase image into moments of topography and local interaction schemes. As a test sample, we have chosen bacteriorhodopsin, which is the light-driven proton pump from *Halobacterium salinarum* (Oesterhelt and Stoeckenius, 1973; Lanyi, 1995; Oesterhelt, 1998). Together with lipids, bacteriorhodopsin

Received for publication 6 December 2000 and in final form 2 March 2001.
Address reprint requests to Martin Stark, Max-Planck-Institut für Biochemie, Abt. Molekulare Strukturbiologie, Am Klopferspitz 18a, D-82152 Martinsried, Germany. Tel.: 49-89-8578-2653; Fax: 49-89-8578-2641; E-mail: stark@biochem.mpg.de.

0006-3495/01/06/3009/10 $2.00

is assembled into the well-defined two-dimensional crystalline lattice of purple membrane (Blaurock and Stoeckenius, 1971). The structure of bacteriorhodopsin has been solved to atomic resolution by electron crystallography and x-ray diffraction (Grigorieff et al., 1996; Pebay-Peyroula et al., 1997; Essen et al., 1998; Luecke et al., 1998; Belrhali et al., 1999), and the surface of purple membrane has been characterized by AFM (Müller et al., 1995; Möller et al., 2000). This allows testing of the accuracy of AFM topographs (Heymann et al., 1999) and correlation of the phase contrast to structural features of purple membrane.

THEORETICAL CONSIDERATIONS

General outline of the concept

In the following, contrast formation in phase imaging is discussed under the focus of interaction and topographical influence. A short outline shall be given first.

The starting point is the relation between phase shift, changes of the amplitude, and dissipated energy as given by Cleveland and co-workers (1998). It is based on the fact that the average energy dissipated per cycle must be equilibrated by the energy imported into the system from the external drive to maintain the oscillation.

From this relation between absolute values, we derive an expression that relates the respective images. In conceiving images as variations around an average value, the emphasis is shifted toward image contrast. Images represent ensembles of measurements on different points under fixed external conditions (scan parameters) rather than a point measurement, where a parameter (usually the mean tip sample distance) is varied.

In a next step, contributions to the phase signal (variations in amplitude and variations of dissipated energy) are discussed. Due to limited response time of the feedback, variations in amplitude occur that are proportional to the first derivative of the topography in the scan direction, assuming homogeneous interaction forces. The dissipated energy is described as surface energy density ϵ effective on the interaction area S between tip and sample. To motivate this view, we discuss a qualitative model for TM-AFM based on cycled, quasi-static force-distance curves, which already shows important sources for energy dissipation.

Finally, the dependence of amplitude variations on the topography, and the dependence of the dissipated energy on the interaction area allow decomposing the phase image into moments of the topography.

The images

We assume the cantilever motion to be stationary on the scale of the time per image pixel. This provides the basis to apply the relation (Eq. 1) between phase shift, amplitude, and energy dissipated in the tip-sample contact (Cleveland et al., 1998):

$$\frac{2Q_{\text{cant}}}{k_{\text{cant}}\omega_{\text{cant}}} E_{\text{diss}} = AA_0 \sin \Phi - A^2, \tag{1}$$

with A the actual amplitude, A_0 the free amplitude, and Φ the phase shift. The cantilever, including its environment, is described by its spring constant k_{cant}, its natural resonant frequency ω_{cant}, and its quality factor Q_{cant}. Quality factors are usually on the order of 1 to 10 (Schäffer et al., 1996; Sader, 1998) for cantilevers immersed in liquid and about two orders of magnitude higher in air. Finally, the net average energy dissipated per cycle in the tip-sample contact is denoted E_{diss}.

Each quantity is decomposed in its average value and its (local) variation; thus

$$E_{\text{diss}} = E^0_{\text{diss}} + \delta E \tag{2a}$$

$$\Phi = 90° + \Phi_0 + \delta\Phi \tag{2b}$$

$$A = A_0(a_0 + \delta a) \tag{2c}$$

Here, δ refers to a difference rather than a differential. The phase shift is measured relative to the free oscillation (90°), thus Φ_0 is the average deviation from 90°, and $\delta\Phi$ denotes variations on that value. A phase shift $\delta\Phi > 0$ is referred to as delayed, because relative to the average the signal is repeated at a time $T\delta\Phi/2\pi$ later (with T as the period length). Correspondingly, $\delta\Phi < 0$ is referred to as advanced. The amplitude is given by the free amplitude A_0 reduced by a factor (set-point) a_0 and variations δa. Using this convention, $\delta\Phi$ is identified with the phase image and δa with the error image. In a similar manner for later use, the topography $H = H_0 + \delta H$, and the interaction area $S = S_0 + \delta S$ are split into their respective averages and the images. For clarity, coordinates (x,y) are omitted.

Expressing A, Φ, and E_{diss} in Eq. 1 with Eqs. 2a–2c yields

$$\frac{2Q_{\text{cant}}}{k_{\text{cant}}\omega_{\text{cant}}A_0^2} (E^0_{\text{diss}} + \delta E) = (a + \delta a)\cos(\Phi_0 + \delta\Phi) - (a_0 + \delta a)^2 \tag{3}$$

Next, the cosine is decomposed, and terms containing $\delta\Phi$ are expanded into their Taylor series. Neglecting terms of the order $o(\delta^2)$, Eq. 3 can be split into two equations, one containing only the averages (Eq. 4a) and the other relating the variations (Eq. 4b):

$$\frac{2Q_{\text{cant}}}{k_{\text{cant}}\omega_{\text{cant}}A_0^2} E^0_{\text{diss}} = a_0 \cos \Phi_0 - a_0^2 \tag{4a}$$

$$\frac{2Q_{\text{cant}}}{k_{\text{cant}}\omega_{\text{cant}}A_0^2} \delta E = (\cos \Phi_0 - 2a_0)\delta a - a_0 \sin \Phi_0 \delta\Phi \tag{4b}$$

Concerning the average values, Eq. 4a yields the same result as Eq. 1. For the phase image $\delta\Phi$, Eq. 4b shows the dependence on the error image δa and on the image (the variations) of dissipated energy δE.

Variations of the amplitude

In TM-AFM, the amplitude is kept at the fixed set-point value by the feedback loop, which uses variations of the amplitude, determined by the physical quantities of topography, interaction, and effective feedback reaction, as input. The error image representing these variations is then converted into the topographical image. As a consequence, the error signal carries no information independent of the topographical image. Variations in the amplitude due to changes in the true sample topography cannot be distinguished from that due to changes in interaction.

Using a proportional-integral feedback mechanism, we obtain Eq. 5 relating the apparent topography and variations in the amplitude:

$$H = \mu[a(x; y) - a_0] + \frac{\lambda}{v}\int_{x_0}^{x}[a(x; y) - a_0]dx, \quad (5)$$

where x is the scan direction, and v is the scan speed. The parameters μ and λ (in matching units) are the proportional and the integral gain, respectively. For a typical image, the proportional part compared with the integral part is negligible because of the gains and small scan speed. Thus, we transform Eq. 5 in the equivalent differential form, obtaining Eq. 6:

$$\delta a = -\frac{v}{\lambda}\,\delta\left(\frac{\partial H}{\partial x}\right) \quad (6)$$

Variations of the amplitude are expressed by changes of the topographical image. Thus, the term containing variations of the amplitude in Eq. 4b describes the influence of the integral feedback.

Interaction, dissipation, and contact area

The dissipated energy E_{diss} in Eq. 1 is a net quantity, subsuming all dissipation channels. A simple model for TM-AFM and the connection between interaction and dissipation is that of a cycled approach-retraction measurement (for comprehensive reviews about force-distance measurements, see Cappella and Dietler 1999; Heinz and Hoh, 1999). A generic force-displacement curve as obtained in contact-mode AFM is depicted in Fig. 1, with the sample surface to the left. As the cantilever approaches the surface, it is deflected because of interaction forces.

Conservative forces, such as electrostatic and van der Waals forces, are time reversible on the time scale of the interaction. Thus, for conservative forces, the retraction trajectory coincides with the approach trajectory. For instance, elastic deformation of a compliant sample results in a flatter slope of the force-displacement curve at tip-sample contact, because the sample is indented, but the trajectories for approach and retraction are identical.

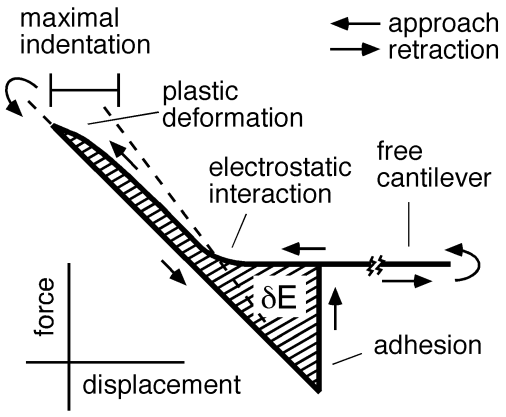

FIGURE 1 Schematic force-displacement curve. The quasistatic force-displacement curve serves as a model for TM-AFM. During the (in TM-AFM periodically repeated) approach-retraction cycle, the tip-sample interaction changes the deflection of the cantilever beam proportional to the force. Differences in the path for approach and retraction equals the amount of energy dissipated due to plastic deformation and adhesion during that cycle.

For dissipative forces, on the other hand, the trajectory is not time reversible on the time scale of the interaction. Thus, dissipative forces result in hysteresis in the approach-retraction cycle. The dissipated work equals the area between the trajectory on approach and on retraction (Cappella and Dietler, 1999; Dürig, 2000). For instance, in the case of plastic deformation (with energy E_{plastic}), the sample is indented, but the deformation does not recover within the tip-sample interaction time. Even the rearrangement of surface charges ($E_{\text{electrostatic}}$) can contribute if the time scale of rearrangement is longer than the interaction time. Evidence for relaxation times on the order of the interaction time is given by Teschke and co-workers (1999). A considerable fraction of energy is dissipated due to adhesive interaction, where the work of adhesion (E_{adhesion}) is used to break the tip-sample contact. Thus, the dissipated energy is described by a sum, Eq. 8:

$$E_{\text{diss}} = E_{\text{adhesion}} + E_{\text{platic}} + E_{\text{electrostatic}} + \ldots \quad (8)$$

In TM-AFM, the full trajectory is cycled as the tip approaches and leaves the surface, driven by a harmonic oscillation. Irreversibility in time associated with dissipation applies also to trajectories in TM-AFM (Dürig, 1999, 2000). In each cycle, the dissipated energy reflects the difference between the path for approach and retraction, which contributes to a phase shift relative to the excitation.

In a first-order approximation, the sample is assumed to recover from one cycle to the following. An additional static distortion adds an additional average dissipated energy to

the system but does not contribute to variations. Regarding TM-AFM under these assumptions, the stationary approach-retraction cycle can directly be considered as a thermodynamic cycle (Fig. 2 *A*). Energy is transferred from a mechanical reservoir (cantilever drive) to a thermal reservoir (bulk sample, tip, and surrounding medium) by a working medium (interaction surface). Conceptually, the mechanical energy is converted into thermal energy by the interaction surface (Fig. 2 *B*). Therefore, the energy dissipated per tapping cycle can be considered as the net energy density integrated over the interaction area.

At this point, it is important to define the interaction surface and interaction area more precisely. The physical processes leading to dissipation happen in a surface-coupled layer. In secondary processes, the energy is distributed and thermally equilibrated in the bulk material of sample, tip, and surrounding media. However, the primary processes are described by quantities defined on the surface, as for example is done for adhesion (see, e.g., Israelachvili, 1991). The choice of the interaction surface, and the energy density coupled to it, must reflect the answer of the coupled layer to the interaction, and consequently to the imported energy. Thus, the energy density describes the local material response, and the interaction area shall be defined as the area that carries the net energy flux. The interaction area depends, in essence, on the local curvature of the sample topography and on the tip geometry. This links our approach to the observations of Behrend et al., 1999.

For further discussion, the interaction area and the dissipation energy density are assumed as independent quantities. For this assumption to hold, contributions due to plastic deformation need to be small compared with area-dependent contributions, such as adhesion. This first-order approximation allows us to identify the interaction area with the geometric contact area S and to write the dissipated energy as product $E_{\mathrm{diss}} = \epsilon S$. With $\epsilon = \epsilon_0 + \delta\epsilon$ and the notations defined above, the dissipation term in Eq. 4b can be written as (Eq. 9):

$$\frac{2Q_{\mathrm{cant}}}{k_{\mathrm{cant}}\omega_{\mathrm{cant}}}\,\delta E_{\mathrm{diss}} = \frac{2Q_{\mathrm{cant}}}{k_{\mathrm{cant}}\omega_{\mathrm{cant}}}\,(\varepsilon_0\delta S + S_0\delta\varepsilon) \qquad (9)$$

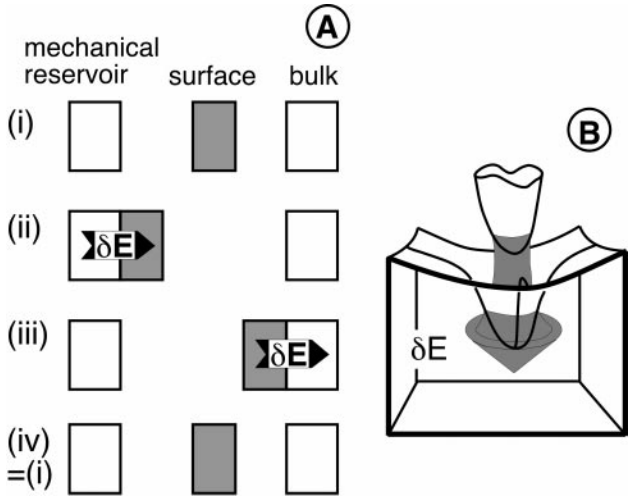

FIGURE 2 Thermodynamic concept of TM-AFM. (*A*) From an energetic point of view, TM-AFM is regarded as a thermodynamic cycle, where energy is taken from a mechanical reservoir (the external drive) and then transferred to a thermal reservoir (bulk, including tip, and surrounding medium). The interaction surface acts as working medium in this cycle. (*B*) Energy transferred from the tip into the bulk is converted on the interaction surface into thermal energy (schematic).

Decomposing the phase image into moments of the topography

After the discussion of terms contributing to the phase shift, we can decompose the phase shift into moments of the topography:

$$\delta\Phi = -\frac{\nu}{\lambda}\frac{\cos\Phi_0 - 2a_0}{a_0\sin\Phi_0}\,\delta\left(\frac{\partial H}{\partial x}\right) + \frac{1}{a_0\sin\Phi_0}\frac{2Q_{\mathrm{cant}}}{k_{\mathrm{cant}}\omega_{\mathrm{cant}}} \times (\varepsilon_0\delta S + S_0\delta\varepsilon) \qquad (10)$$

Thus, correcting the phase image for influences of the error image (the derivative of the topography in scan direction, denoted first order) and the interaction area (denoted second order), the image of the dissipative interaction energy density is obtained, which characterizes sample properties.

In a typical TM-AFM experiment, the average quantities are not accessible as absolute values. This is especially true for the absolute phase shift in liquid, the gains, and the mean dissipated energy. Thus, we express the image of the energy densities as proportional (γ) to the sum of the other images (Eq. 11):

$$\gamma\delta\varepsilon = \delta\Phi - \alpha\delta\left(\frac{\partial H}{\partial x}\right) - \beta\delta S, \qquad (11)$$

where the coefficients α and β are determined using additional knowledge about the experiment. Especially symmetries help to find adequate approximations for the coefficients in Eq. 11. The symmetry of the interaction area follows the symmetry of the topography, whereas the symmetry of the derivative is different, that is, assuming symmetric topography yields a symmetric interaction area, whereas the derivative of the topography in scan direction is anti-symmetrical.

MATERIALS AND METHODS

Atomic force microscopy and imaging

A commercial AFM (Nanoscope Multimode IIIa, Digital Instruments, Santa Barbara, CA) equipped with a 12-μm piezo scanner (E-scanner) was operated in standard tapping mode (tapping amplitude as input in the feedback loop) and used with a homebuilt phase-detection setup (Stark and

Guckenberger, 1999). After thoroughly cleaning the tapping-mode liquid cell with a dish cleaner, rinsing it several times alternately with ethanol and ultra-pure water (≥18 MΩ/cm, MiliQ system, Millipore, Eschborn, Germany), and drying it in a nitrogen stream, the cell was exposed to ultraviolet light to obtain a hydrophilic surface especially in the vicinity of the cantilever chip mounting. The latter procedure suppresses the formation of air bubbles close to the cantilever. No O-ring seal was used.

To reduce the background noise level, the light path of the AFM was regularly cleaned. Dust in the light path produced major contributions to the noise, particularly adding instabilities to the signal. Acoustic noise was blocked with a hood, and the setup was allowed to thermally equilibrate for several hours. The noise level can be estimated by observing the photodiode signal directly on an oscilloscope.

V-shaped silicon nitride cantilevers with nominal spring constants around 0.65 N/m (100-μm length, oxide-sharpened tip; type OMCL-TR800PSA, manufactured by Olympus Optical Co., Tokyo, Japan) were used. In fluid, the resonance frequency was ~20 kHz (28 kHz for another batch) as determined by thermal noise spectra. In the case of 20 kHz, the oscillation of the cantilever is not supported by a resonance of the fluid-cell; thus, driving voltages were in the range of 1 V, yielding tapping amplitudes of 1–5 nm. Typically, set-point values were chosen between 0.85 and 0.95 of the free amplitude. Preferably, scan speed was adjusted to two scan lines per second, and a maximum of four lines corresponding to five contact events per image pixel at 20-kHz lever frequency.

Sample and sample preparation

Purple membrane of *Halobacterium salinarum* strain ET1001 was isolated as decribed by Oesterhelt and Stoeckenius (1974). Freshly cleaved Muscovite mica (BAL-TEC AG, Balzers, Liechtenstein) was used as support, glued to a Teflon-laminated mounting. Buffer solutions (10 mM Tris, 300 mM KCl) were always freshly prepared with ultra-pure water and adjusted to pH 8.2. After 15 min of adsorption, the samples were gently rinsed to remove weakly adsorbed membranes. For a detailed experimental description see Möller et al. (1999).

Image processing

The images (512 × 512 pixels) were imported as raw data into the Semper image-processing package (Saxton et al., 1979). Height and phase measurements of features in the images were performed by applying masks to the whole images. Derivatives of the topographical images were determined by applying anti-symmetric standard convolution filters in real space. Correlation averaging was done by cross-correlating a selected well-preserved unit cell of the topograph with the whole topograph (Saxton and Baumeister, 1982). The positions of the correlation peaks were used to extract the ensemble of unit cells, which was averaged. For better visualization, the obtained averages were enlarged by interpolation in Fourier-space by a factor of four. The sequence of operations (derivation, averaging, and interpolation) was exchangeable without significant influence on the resulting images (better than 99% cross-correlation).

Routines calculating the contact area were adopted from a procedure for estimation of the tip radius (Bonnet et al., 1994). With a first estimate for the tip radius, the original topographical image is restored to remove distortion due to the tip shape (often and improperly, this process is referred to as tip deconvolution) and thus yields an approximation for the true topography of the sample. The obtained restoration is again degraded (referred to as tip convolution), using the same tip parameters. The difference image (the original image minus the restored-degraded image) is quantified by the overall standard deviation. According to Bonnet, the relation between the standard deviation and the estimated tip radius has two almost linear regimes. The tip radius at the transition between the two regimes gives an estimate for the largest tip consistent with the image data.

For each pixel, the overlap of the sample topography and the estimated tip enlarged by a fixed and small (compared with the tip radius) interaction depth was calculated, yielding the geometric interaction area. For small values, the interaction depth acts only like a scaling factor for the interaction area.

RESULTS

Low-magnification data

Purple membrane adsorbed on mica exhibits flat, roundly shaped patches (Fig. 3 *A*; image size is 1.61 μm) with a height of 6.3 ± 0.1 nm. Occasionally, the purple membranes are surrounded by a lipid bilayer with an apparent height of 3.8 ± 0.3 nm. Whereas the membrane and the lipid are decorated by protrusions of unknown origin, the mica substrate is almost clean. At this magnification, no significant substructure can be seen on the purple membrane. Topographical variations are averaged by the pixel size (3.15 nm). The spacing of the crystalline lattice (6.2 nm) is at the limit of the nominal resolution of 6.3 nm, and the membrane appears flat.

The phase image presented in Fig. 3 *B* is unprocessed. The line-wise averaged difference between the phase shift on mica and that on purple membrane (PM) is given in Fig. 3 *C*. Relative to mica the phase-shift on purple membrane is on average advanced by −2.0 ± 1.4°. Striking line-wise variations of the phase shift are especially obvious on mica. Strong shadowing in the phase image occurs at step-like features, such as the rim of the membrane and the decorating protrusions (see *arrows* in Fig. 3 *B*). At the rising edge (scan direction is from the left to the right), the phase shift is advanced (dark in the image), and at the falling edge it is delayed.

High-resolution data

At higher magnification, the crystalline substructure is revealed (Fig. 4, extracellular side). Already in the raw data

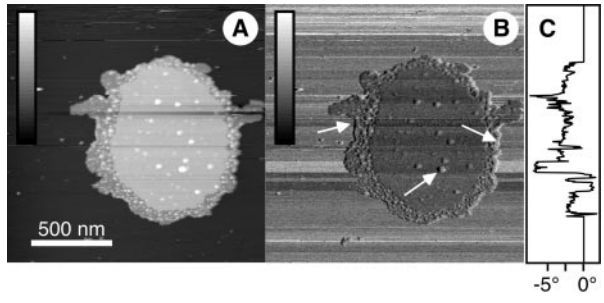

FIGURE 3 Purple membrane in buffer solution, overview. (*A*) The topographical image shows a membrane patch adsorbed on mica, and surrounded by a lipid rim. Protrusions of unknown origin decorate the membrane and the lipid. (*B*) In the phase image, membrane and mica exhibit a clear contrast. A shadowing in scan direction (left to right) occurs in the phase image at positions where large changes are present in the topography (see *arrows*). (*C*) The difference in phase shift between purple membrane and mica averaged along the scan lines emphasizes the phase contrast between the two materials. Scales: in *A*, the height spans 11 nm (black to white); in *B*, the phase shift spans 15°; scale bar, 500 nm.

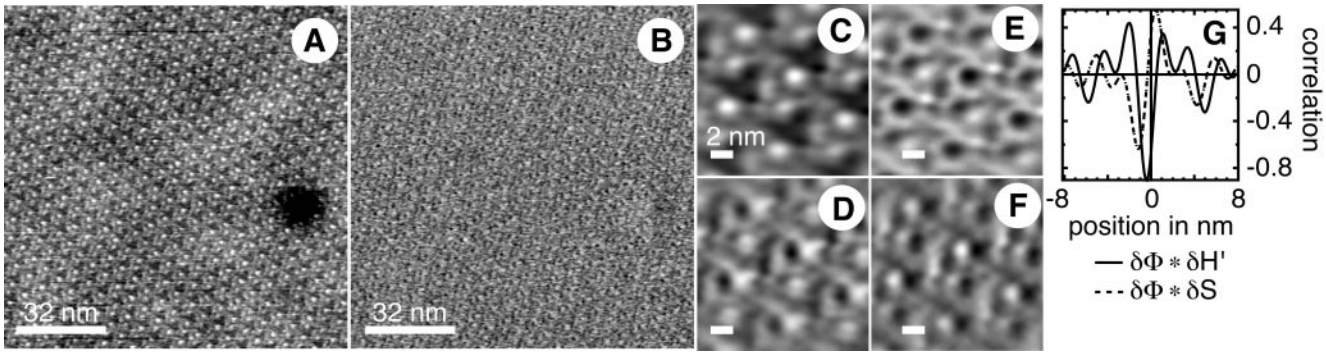

FIGURE 4 High-resolution images of the extracellular side of purple membrane, raw and processed data. (*A* and *B*) Raw data: topography (*A*) and the phase shift (*B*); the trimers of bacteriorhodopsin and the periodicity of the arrangement are clearly resolved. A point defect in the crystalline lattice is visible as a black spot in the topography. The scale bar is 32 nm, and the gray scale from black to white represents 1 nm (*A*) and 7.5° (B), respectively. (*C–G*) Processed data. In the average topography (*C*), the trimer (bright) is evident, and lipid fills the inter-space between the trimers (dark). The phase image (*D*) shows an asymmetry along the scan direction (left to right). Over the elevated parts, the phase changes most. This has to be compared with the geometric contact area (*E*) and to the first derivative in scan direction (*F*), which are both calculated from the averaged topography (for details about the calculation, see Materials and Methods). (*G*) Cross-correlating the phase image with the first derivative in scan direction ($\delta\Phi^*\delta H'$, ——) and with the interaction area ($\delta\Phi^*\delta S$, — — —) demonstrates the strong influence of the topography. Here, only the horizontal cross sections along the centers of the images are shown. Scale bar, 2 nm (*C–F*); the gray scale (black to white) represents 0.65 nm (*C*), 3° (*D*), ± 2.5 nm^2 around 3.93 nm^2 (*E*), and ± 0.5 (*F*).

(topography in Fig. 4 *A*, phase shift in 4 *B*) the bacteriorhodopsin trimers, arranged in a trigonal lattice, are observed. Correlation averages ($n = 501$) are presented in Fig. 4, *C* and *D* (topography and phase shift, respectively).

The lattice spacing is determined to be 6.2 ± 0.2 nm. The trimer appears as three large protrusions with $\sim 2.4 \pm 0.2$ nm in diameter and separated by 2.8 ± 0.2 nm. Additionally, three small protrusions separated by 1.7 ± 0.2 nm connect the trimers. The values are derived from Fourier-interpolated data. Lipid fills the inter-space between the trimers. The maximum height difference in the averaged topography is 0.5 ± 0.1 nm whereas the highest and the lowest point are laterally separated roughly 2 nm.

Along with the averaging routine, the lateral phase residual resolution was calculated (according to Unser et al., 1987; Schabert and Engel, 1994). For the topography, the resolution was limited by the pixel size (0.5 nm) to 1.0 nm; for the phase image, 1.4 nm was obtained. From these numbers, the tip radius for the outermost, sensing tip can be estimated to be ≤ 1 nm.

The averaged phase image (maximum phase difference is 2.78°) exhibits strong shadowing in the scan direction (left to right). Furthermore, the symmetry of the averaged phase image differs from that of the topography. Over protrusions, the phase image $\delta\Phi$ flips contrast, whereas the lipid background is almost uniform.

Image analysis of the averaged high-resolution data

In this subsection, the concept developed in theoretical considerations is applied to the high-resolution data as a model system.

Based on the averaged topography, the interaction area, and the first derivative in the scan direction were calculated (Fig. 4, *E* and *F*, respectively). To calculate the interaction area, the tip radius was estimated to be 0.6 nm. At that value, the difference between the original image, and the restored-degraded image starts to become significant (see Materials and Methods). In Fig. 5, the resulting standard deviation for the difference image (original topographical image minus the restored-degraded image) is plotted versus the estimate for the tip radius.

Fig. 4 *G* shows the cross-correlation of the phase image with the first derivative and the interaction area, respectively. The phase is essentially anti-correlated with the first derivative. From a cross section along the marked line, a

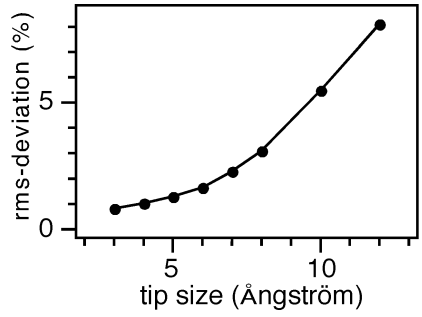

FIGURE 5 Estimation of the tip radius. To estimate the tip radius, the original image is first corrected for the influence of an assumed tip and then again degraded using the same tip. Both images, the original and the restored-degraded image, differ. The standard deviation (rms deviation) for the difference image is plotted versus the radius of the assumed tip. From the resulting curve, the tip radius was estimated to be roughly 0.6 nm, because at that value, a change of the assumed tip radius starts to significantly influence the difference image. For details see Materials and Methods.

shift of the minimal correlation coefficient (−0.91; best anti-correlation) to the left of the image center can bee seen. At the origin, the correlation coefficient is −0.66. Correlating to the interaction area yields a correlation coefficient of 0.42 at the origin and a maximum of 0.56 shifted to the right. Because phase shift and topography are recorded simultaneously and the acquisition of the phase signal is faster than the pixel time, collocation of all signals is assumed; i.e., the origin is in the center of each image.

In a first step, a term proportional to the first derivative is subtracted from the phase image in such a way that the standard deviation of the obtained image $\delta\Phi_1 = \delta\Phi - \alpha\delta(\partial H/\partial x)$ is minimized. The effect of this operation is demonstrated in Fig. 6 *A*. Along the line indicated, the cross section (Fig. 6 *B*) clearly shows the difference between the resulting and the original phase image. Along with this, the cross-correlation coefficient of $\delta\Phi_1$ with the first derivative becomes zero at the origin (Fig. 6 *E*). On the other hand, the cross-correlation of $\delta\Phi_1$ with the interaction surface exhibits its maximum of 0.55 at the origin. Thus, correcting for the derivative yields an image with symmetry close to that of the interaction surface and increased correlation coefficient.

Second, a term proportional to the interaction area is subtracted, again minimizing the standard deviation of the obtained image $\delta\Phi_2 = \delta\Phi_1 - \beta\delta S$. The resulting image, shown in Fig. 6 *C*, is identified with the unscaled approximation of the dissipative interaction energy density $\delta\epsilon$. Again, the effect of the operation is visualized in cross sections (Fig. 6 *D*).

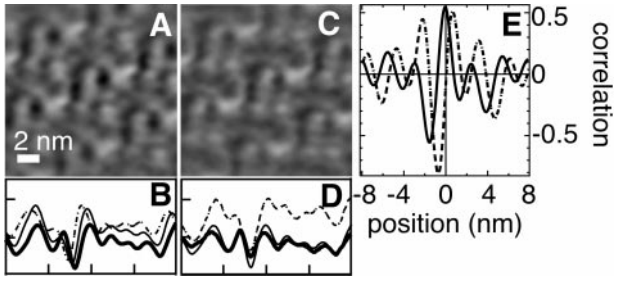

FIGURE 6 Steps in the image analysis of the phase image. (*A*) The influence of the derivative of the topography in scan direction is subtracted from the phase image, yielding $\delta\Phi_1$. (*B*) Cross sections along the central horizontal line visualize the effect: the resulting image (*thick black line*), the phase shift (*thin black line*), and the derivative in the scan direction (*thin broken line*). (*C*) Further correction of *A* for the contact area δS leads to an estimate for the interaction. (*D*) Again, the effect is visualized in cross sections: the interaction energy density image (*thick black line*), the phase shift corrected for the first derivative (*thin black line*), and the interaction area (*thin broken line*). Scale bar, 2 nm; the gray scales are the same as in Fig. 4 *D*; i.e., 3° (the unit is set for consistency to degree). (*E*) Cross-correlating the phase image corrected for the derivative with the derivative (— — —) leads to an almost antisymmetric curve that is almost zero at (0,0), whereas the cross-correlation with the interaction area (——) has a maximum at (0,0). Here, only the horizontal cross sections along the centers of the images are shown.

DISCUSSION AND CONCLUSIONS

Low-magnification data

In the low-magnification data (Fig. 3), mica and purple membrane can clearly be distinguished in the phase image. The shadowing at edges is clearly related to the limited feedback response, whereas the striking line-wise variations are most probably related to instabilities of the tip oscillation itself (Anczykowski et al., 1998; San Paulo and García, 2000). Tip contamination is another possible reason for the stripes in the phase image, but with the same tip, a reliable resolution of 1.32 nm was achieved later (not shown).

At this scan size, variations of the amplitude due to the structure of bacteriorhodopsin are averaged by the large pixel size, and the membrane appears flat. Therefore, the image contrast is dominated by interaction area and dissipation energy density. In accordance with quasi-static data (Müller et al., 1999a), forces are almost balanced at the given buffer conditions for purple membrane, whereas on mica a residual adhesion remains. Therefore, under the given conditions, more energy is dissipated on mica than on purple membrane.

High-resolution data

The high-resolution data (Fig. 4) are in good agreement with data recorded recently in contact-mode AFM (Müller et al., 1999b) and TM-AFM (Möller et al., 1999), and show the well-preserved structure of the bacteriorhodopsin trimers. This supports the assumption that deformation induced by the tip-sample contact is negligible.

The shadowing as well as the anti-symmetry of the phase image with respect to the topographical image, point to a strong influence of the topography on the phase image. Thus, despite the high resolution, properties of image features cannot be related to the phase image without further analysis. Because the tip size is comparable to structural length scales and to the resolution, the two important parameters, interaction area and derivative of the topography in scan direction, contribute comparable strongly, so an analysis has to account for both effects.

Image analysis of the averaged high-resolution data

The correlation coefficients (Fig. 4 *G*) emphasize the need for image analysis. Correcting the phase image for contributions of amplitude variations ($\delta(\partial H/\partial x)$, derivative of the topography in scan direction) resulted in an image ($\delta\Phi_1$) with altered symmetry. Furthermore, the relation with the interaction area image becomes more pronounced. The shape of the remaining structure in the cross-correlation of the corrected phase shift with the derivative in scan direction is a consequence of the symmetries involved. A cross-

correlation between a symmetric function and an anti-symmetric one leads again to an anti-symmetric cross-correlation function. The limited feedback response affects the phase image in the same manner over the whole image; thus, a uniform linear correction as performed for Fig. 6 is appropriate.

In the theoretical considerations, the energy dissipation was linearly approximated by a product energy density times interaction area. The underlying assumption, that plastic deformation is small, is reasonable, because the data are in good agreement with previous studies (see above). This approximation led to the dissipation energy density image $\delta\Phi_2$ (Fig. 6 *C*).

Nevertheless, the assumption of independence of the parameters energy density ϵ and interaction area S (and with it the linearity) needs further discussion. As a tool to address this point, and to qualify the coupling of ϵ and S, we propose a relation plot (Fig. 7 *A*), which allows us to estimate the functional dependence of the two variables. For each image pixel (x,y), the phase shift corrected for the influence of amplitude variations, $\delta\Phi_1(x,y)$, and the interaction area $\delta S(x,y)$ are transferred into a map $n(\delta S,\delta\Phi_1)$. The values n of the map count the number of pixels with value $\delta\Phi_1$ and δS. Here, the ranges for $\delta\Phi_1$ and δS are divided into 64 bins each. For a single functional dependence $\delta\Phi_1(\delta S)$, the appertaining curve will be obtained. Otherwise, for features with different functional dependencies, the structure in the relation plot is a superposition of curves, each of them representing $\delta\Phi_1(\delta S)$ for the respective set of features in the topographical image.

In the case presented, the obtained relation plot is almost linear, which justifies the linear approximation. Despite the overall linear behavior, areas deviating from linearity are identified. These structures can be related to features in the topography. Along with sorting the pairs $(\delta S,\delta\Phi_1)$, it can be determined which structure $(\delta S,\delta\Phi_1)$ belongs to a given topographical feature (i.e., protein or lipid). Vice versa, those pixels with pairs $(\delta S,\delta\Phi_1)$ belonging to a structure in the relation plot can be addressed in the topography.

Three areas are highlighted in the relation plot (Fig. 7 *A*), and the associated topographical features (Fig. 7 *B*) are protein (1), lipid (3), and the material in between (2), which cannot be identified unambiguously. Regions not addressed by one of the highlighted parts of the relation plot cover the rest (black in Fig. 7 *B*). For the three features, a linear approximation seems appropriate, but with different parameters. Thus, it can be concluded that the protein differs from the lipid in the dependence $\delta\Phi_1(\delta S)$. This gives a strong indication for a different interaction scheme for protein and lipid.

However, the results show a low difference in the interaction, which may be a particular feature of the sample investigated. In a more general case, plastic or viscoelastic contributions are expected to become prominent in the relation plot.

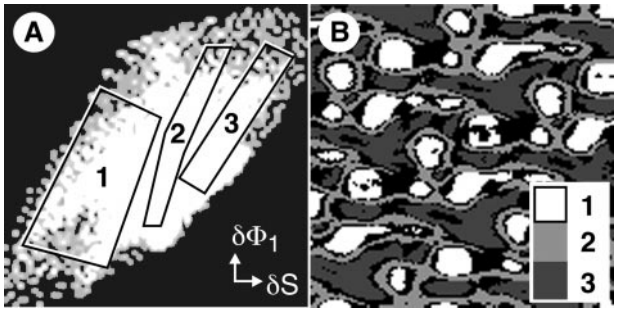

FIGURE 7 Relation plot-phase shift corrected for the first derivative in scan direction, $\delta\Phi_1$, versus interaction area, δS. (*A*) The number of pixels with a pair of values $(\delta S,\delta\Phi_1)$ is plotted in a diagram. From this diagram, the functional dependence of $\delta\Phi_1$ on δS is estimated. Sub-regions of this plot, highlighted and numbered in *A*, correspond to features in the topography, shown in *B*. Region 1 (white) corresponds to the protein trimer, region 2 (light gray) to the ambiguous intermediate regions, and region 3 (dark gray) corresponds to lipid. The black background covers the rest. In *A*, the δS axis covers values of ± 2.5 nm^2 around 3.93 nm^2, the $\delta\Phi_1$ 3° (as in Fig. 6 *A*). The colors represent the counts: dark corresponds to low number of counts and bright to a number of counts >6.

Conclusions

Phase imaging in TM-AFM provides additional information on material properties. An interpretation of phase images has necessarily to account for influences of the topography. This is especially important in the case of biological specimens, where the surface corrugation is in general in the size of the AFM tip.

The topography is found responsible for at least two-thirds of the image contrast in the case of high-resolution phase images (1.4-nm lateral resolution in the phase image) of purple membrane. Our analysis showed that decomposing the phase image into moments of the topography, i.e., the first derivative in scan direction and the geometric contact area, allows us to separate interaction from topography. Based on these results, we propose the relation plot as an instrument to distinguish different interaction schemes.

We thank G. Büldt for the sample and A. Engel for his efforts.

This work was supported by the Deutsche Forschungsgemeinschaft (SFB 266) and the German Academic Exchange Service (Doktorandenstipendium HSP III).

REFERENCES

Anczykowski, B., J. P. Cleveland, D. Krüger, V. Elings, and H. Fuchs. 1998. Analysis of the interaction mechanisms in dynamic-mode sfm by means of experimental-data and computer-simulation. *Appl. Phys. A Mater. Sci. Process.* 66:S885–889.

Anczykowski, B., B. Gotsmann, H. Fuchs, J. P. Cleveland, and V. B. Elings. 1999. How to measure energy dissipation in dynamic mode atomic force microscopy. *Appl. Surface Sci.* 140:376–382.

Anczykowski, B., D. Krüger, and H. Fuchs. 1996. Cantilever dynamics in quasinoncontact force microscopy: spectroscopic aspects. *Phys. Rev. B Condensed Matter*. 53:15485–15488.

Behrend, O. P., L. Odoni, J. L. Loubet, and N. A. Burnham. 1999. Phase imaging: deep or superficial. *Appl. Phys. Lett.* 75:2551–2553.

Belrhali, H., P. Nollert, A. Royant, C. Menzel, J. P. Rosenbusch, E. M. Landau, and E. Pebay-Peyroula. 1999. Protein, lipid and water organization in bacteriorhodopsin crystals: a molecular view of the purple membrane at 1.9 Ångstrom resolution. *Struct. Fold. Design.* 7:909–917.

Bielefeldt, H., and F. J. Giessibl. 1999. A simplified but intuitive analytical model for intermittent contact-mode force microscopy based on Hertzian mechanics. *Surface Sci.* 440:L863–L867.

Binnig, G., C. F. Quate, and C. Gerber. 1986. Atomic force microscopy. *Phys. Rev. Lett.* 56:930–933.

Blaurock, A. E., and W. Stoeckenius. 1971. Structure of purple membrane. *Nat. New Biol.* 233:152–154.

Bonnet, N., S. Dongmo, P. Vautrot, and M. Troyon. 1994. A mathematical morphology approach to image-formation and image-restoration in scanning tunneling and atomic-force microscopies. *Microsc. Microanal. Microstruct.* 5:477–487.

Burnham, N. A., O. P. Behrend, F. Oulevey, G. Gremaud, P.-J. Gallo, D. Gourdon, E. Dupas, A. J. Kulik, H. M. Pollock, and G. A. D. Briggs. 1997. How does a tip tap? *Nanotechnology.* 8:67–75.

Cappella, B., and G. Dietler. 1999. Force-distance curves by atomic force microscopy. *Surface Sci. Rep.* 34:1–104.

Chen, X., S. L. McGurk, M. C. Davies, C. J. Roberts, K. M. Shakesheff, S. J. B. Tendler, P. M. Williams, J. Davies, A. C. Dawkes, and A. Domb. 1998. Chemical and morphological analysis of surface enrichment in a biodegradable polymer blend by phase-detection imaging atomic-force microscopy. *Macromolecules.* 31:2278–2283.

Cleveland, J. P., B. Anczykowski, A. E. Schmid, and V. B. Elings. 1998. Energy-dissipation in tapping-mode atomic-force microscopy. *Appl. Phys. Lett.* 72:2613–2615.

Czajkowsky, D. M., M. J. Allen, V. Elings, and Z. F. Shao. 1998. Direct visualization of surface-charge in aqueous-solution. *Ultramicroscopy.* 74:1–5.

Czajkowsky, D. M., and Z. F. Shao. 1998. Submolecular resolution of single macromolecules with atomic force microscopy. *FEBS Lett.* 430: 51–54.

Dorn, I. T., R. Eschrich, E. Seemüller, R. Guckenberger, and R. Tampé. 1999. High-resolution AFM-imaging and mechanistic analysis of the 20 S proteasome. *J. Mol. Biol.* 288:1027–1036.

Drake, B., C. B. Prater, A. L. Weisenhorn, S. A. C. Gould, T. R. Albrecht, C. F. Quate, D. S. Cannell, H. G. Hansma, and P. K. Hansma. 1989. Imaging crystals, polymers, and processes in water with the atomic force microscope. *Science.* 243:1586–1588.

Dürig, U. 1999. Conservative and dissipative interactions in dynamic force microscopy. *Surface Interface Anal.* 27:467–473.

Dürig, U. 2000. Interaction sensing in dynamic force microscopy. *N. J. Phys. http://www.njp.org/.* 2:5.1–5.12.

Essen, L. O., R. Siegert, W. D. Lehmannn, and D. Oesterhelt. 1998. Lipid patches in membrane protein oligomers: Crystal structure of the bacteriorhodopsin-lipid complex. *Proc. Natl. Acad. Sci. U.S.A.* 95: 11673–11678.

García, R., and A. San Paulo. 2000. Dynamics of a vibrating tip near or in intermittent contact with a surface. *Phys. Rev. B.* 61:R13381-R13384.

García, R., J. Tamayo, and A. San Paulo. 1999. Phase contrast and surface energy hysteresis in tapping mode scanning force microsopy. *Surface Interface Anal.* 27:312–316.

Gil, A., J. Colchero, M. Luna, J. Gomez-Herrero, and A. M. Baro. 2000. Adsorption of water on solid surfaces studied by scanning force microscopy. *Langmuir.* 16:5086–5092.

Grandbois, M., H. Clausens-chaumann, and H. Gaub. 1998. Atomic-force microscope imaging of phospholipid-bilayer degradation by phospholipase a(2). *Biophys. J.* 74:2398–2404.

Grigorieff, N., T. A. Ceska, K. H. Downing, J. M. Baldwin, and R. Henderson. 1996. Electron-crystallographic refinement of the structure of bacteriorhodopsin. *J. Mol. Biol.* 259:393–421.

Hansma, P. K., J. P. Cleveland, M. Radmacher, D. A. Walters, P. E. Hillner, M. Bezanilla, M. Fritz, D. Vie, H. G. Hansma, and C. B. Prater. 1994. Tapping mode atomic-force microscopy in liquids. *Appl. Phys. Lett.* 64:1738–1740.

Heinz, W. F., and J. H. Hoh. 1999. Spatially resolved force spectroscopy of biological surfaces using the atomic force microscope. *Trends Biotechnol.* 17:143–150.

Heymann, J. B., D. J. Müller, E. M. Landau, J. P. Rosenbusch, E. Pebay-Peyroula, G. Büldt, and A. Engel. 1999. Charting the surfaces of the purple membrane. *J. Struct. Biol.* 128:243–249.

Hillenbrand, R., M. Stark, and R. Guckenberger. 2000. Higher-harmonics generation in tapping-mode atomic-force microscopy: Insights into the tip-sample interaction. *Appl. Phys. Lett.* 76:3478–3480.

Hoh, J. H., G. E. Sosinsky, J. P. Revel, and P. K. Hansma. 1993. Structure of the extracellular surface of the gap junction by atomic-force microscopy. *Biophys. J.* 65:149–163.

Israelachvili, J. 1991. Intermolecular and Surface Forces. Academic Press, London.

Kuznetsov, Y. G., A. J. Malkin, T. A. Land, J. J. Deyoreo, A. P. Barba, J. Konnert, and A. McPherson. 1997. Molecular resolution imaging of macromolecular crystals by atomic-force microscopy. *Biophys. J.* 72: 2357–2364.

Lanyi, J. K. 1995. Bacteriorhodopsin as a model for proton pumps. *Nature.* 375:461–463.

Luecke, H., H. T. Richter, and J. K. Lanyi. 1998. Proton transfer pathways in bacteriorhodopsin at 2.3 Ångstrom resolution. *Science.* 280: 1934–1937.

Magonov, S. N., V. Elings, and M. H. Whangbo. 1997. Phase imaging and stiffness in tapping-mode atomic-force microscopy. *Surface Sci.* 375: L385–391.

Malkin, A. J., Y. G. Kuznetsov, and A. McPherson. 1997. An in-situ AFM investigation of catalase crystallization. *Surface Sci.* 393:95–107.

McMaster, T. J., M. Berry, A. P. Corfield, and M. J. Miles. 1999. Atomic force microscopy of the submolecular architecture of hydrated ocular mucins. *Biophys. J.* 77:533–541.

Möller, C., M. Allen, V. Elings, A. Engel, and D. J. Müller. 1999. Tapping-mode atomic force microscopy produces faithful high resolution images of protein surfaces. *Biophys. J.* 77:1150–1158.

Möller, C., G. Büldt, N. A. Dencher, A. Engel, and D. J. Müller. 2000. Reversible loss of crystallinity on photobleaching purple membrane in the presence of hydroxylamine. *J. Mol. Biol.* 301:869–879.

Müller, D. J., G. Büldt, and A. Engel. 1995. Force-induced conformational change of bacteriorhodopsin. *J. Mol. Biol.* 249:239–243.

Müller, D. J., and A. Engel. 1999. Voltage and pH-induced channel closure of porin OmpF visualized by atomic force microscopy. *J. Mol. Biol.* 285:1347–1351.

Müller, D. J., D. Fotiadis, S. Scheuring, S. A. Müller, and A. Engel. 1999a. Electrostatically Balanced Subnanometer Imaging of Biological Specimen by Atomic Force Mircoscope. *Biophys. J.* 76:1101–1111.

Müller, D. J., H. J. Sass, S. A. Müller, G. Büldt, and A. Engel. 1999b. Surface structures of native bacteriorhodopsin depend on the molecular packing arrangement in the membrane. *J. Mol. Biol.* 285:1903–1909.

Noy, A., C. H. Sanders, D. V. Vezenov, S. S. Wong, and C. M. Lieber. 1998. Chemically-sensitive imaging in tapping mode by chemical force microscopy - relationship between phase-lag and adhesion. *Langmuir.* 14:1508–1511.

Oesterhelt, D. 1998. The structure and mechanism of the family of retinal proteins from halophilic archaea. *Curr. Opin. Struct. Biol.* 8:489–500.

Oesterhelt, F., D. Oesterhelt, M. Pfeiffer, A. Engel, H. E. Gaub, and D. J. Müller. 2000. Unfolding pathways of individual bacteriorhodopsins. *Science.* 288:143–146.

Oesterhelt, D., and W. Stoeckenius. 1973. Functions of a new photoreceptor membrane. *Proc. Natl. Acad. Sci. U.S.A.* 70:2853–2857.

Oesterhelt, D., and W. Stoeckenius. 1974. Isolation of the cell membrane of *Halobacterium halobium* and its fraction into red and purple membrane. *Methods Enzymol.* 31:667–678.

Pebay-Peyroula, E., G. Rummel, J. P. Rosenbusch, and E. M. Landau. 1997. X-ray structure of bacteriorhodopsin at 2.5 angstroms from microcrystals grown in lipidic cubic phases. *Science.* 277:1676–1681.

Putman, C. A. J., K. O. Van der Werf, B. G. De Grooth, N. F. Van Hulst, and J. Greve. 1994. Tapping mode atomic-force microscopy in liquid. *Appl. Phys. Lett.* 64:2454–2456.

Sader, J. E. 1998. Frequency-response of cantilever beams immersed in viscous fluids with applications to the atomic-force microscope. *J. Appl. Phys.* 84:64–76.

San Paulo, A., and R. García. 2000. High-resolution imaging of antibodies by tapping-mode atomic force microscopy: attractive and repulsive tip-sample interaction regimes. *Biophys. J.* 78:1599–1605.

Sarid, D., T. G. Ruskell, R. K. Workman, and D. Chen. 1996. Driven nonlinear atomic force microscopy cantilevers: from noncontact to tapping modes of operation. *J. Vac. Sci. Technol. B.* 14:864–867.

Saxton, W. O., and W. Baumeister. 1982. The correlation averaging of a regularly arranged bacterial cell envelope protein. *J. Microsc.* 127: 127–138.

Saxton, W. O., T. J. Pitt, and M. Horner. 1979. Digital image processing: the semper system. *Ultramicroscopy.* 4:343–354.

Schabert, F. A., and A. Engel. 1994. Reproducible acquisition of *Escherichia coli* porin surface topographs by atomic-force microscopy. *Biophys. J.* 67:2394–2403.

Schabert, F. A., C. Henn, and A. Engel. 1995. Native *escherichia coli* ompf porin surfaces probed by atomic-force microscopy. *Science.* 268:92–94.

Schäffer, T. E., J. P. Cleveland, F. Ohnesorge, D. A. Walters, and P. K. Hansma. 1996. Studies of vibrating atomic-force microscope cantilevers in liquid. *J. Appl. Phys.* 80:3622–3627.

Stark, R. W., and W. M. Heckl. 2000. Fourier transformed atomic force microscopy: tapping mode atomic force microscopy beyond the Hookian approximation. *Surface Sci.* 457:219–228.

Stark, M., and R. Guckenberger. 1999. Fast low-cost phase detection setup for tapping-mode atomic force microscopy. *Rev. Sci. Instrum.* 70: 3614–3619.

Stark, M., R. W. Stark, W. M. Heckl, and R. Guckenberger. 2000. Spectroscopy of the anharmonic cantilever oscillations in tapping-mode atomic-force microscopy. *Appl. Phys. Lett.* 77:3293–3295.

Tamayo, J., and R. García. 1996. Deformation, contact time, and phase-contrast in tapping mode scanning force microscopy. *Langmuir.* 12: 4430–4435.

Tamayo, J., and R. García. 1997. Effects of elastic and inelastic interactions on phase-contrast images in tapping-mode scanning force microscopy. *Appl. Phys. Lett.* 71:2394–2396.

Teschke, O., E. F. de Souza, and G. Ceotto. 1999. Double layer relaxation measurements using atomic force microscopy. *Langmuir*. 15: 4935–4939.

Thomann, Y., H. J. Cantow, G. Bar, and M. H. Whangbo. 1998. Investigation of morphologies and nanostructures of polymer blends by tapping mode phase imaging. *Appl. Phys. A Mater. Sci. Proc.* 66:S1233–S1236.

Unser, M., B. L. Trus, and A. C. Steven. 1987. A new resolution criterion based on spectral signal-to-noise ratios. *Ultramicroscopy.* 23:39–52.

Van Noort, S. J. T., K. O. Van der Werf, B. G. de Grooth, N. F. Van Hulst, and J. Greve. 1997. Height anomalies in tapping mode atomic-force microscopy in air caused by adhesion. *Ultramicroscopy.* 69:117–127.

Viani, M. B., L. I. Pietrasanta, J. B. Thompson, A. Chand, I. C. Gebeshuber, J. H. Kindt, M. Richter, H. G. Hansma, and P. K. Hansma. 2000. Probing protein-protein interactions in real time. *Nat. Struct. Biol.* 7:644–647.

Vinckier, A., P. Gervasoni, F. Zaugg, U. Ziegler, P. Lindner, P. Groscurth, A. Plückthun, and G. Semenza. 1998. Atomic-force microscopy detects changes in the interaction forces between GroEl and substrate proteins. *Biophys. J.* 74:3256–3263.

Whangbo, M. H., G. Bar, and R. Brandsch. 1998. Description of phase imaging in tapping mode atomic-force microscopy by harmonic approximation. *Surface Sci.* 411:L794–801.

Winkler, R. G., J. P. Spatz, S. Sheiko, M. Moller, P. Reineker, and O. Marti. 1996. Imaging material properties by resonant tapping-force microscopy: a model investigation. *Phys. Rev. B Condensed Matter*. 54:8908–8912.

Yang, J., J. X. Mou, and Z. F. Shao. 1994. Molecular resolution atomic-force microscopy of soluble-proteins in solution. *Biochim. Biophys. Acta.* 1199:105–114.

Yip, C. M., M. R. DeFelippis, B. H. Frank, M. L. Brader, and M. D. Ward. 1998. Structural and morphological characterization of ultralente insulin crystals by atomic-force microscopy: evidence of hydrophobically driven assembly. *Biophys. J.* 75:1172–1179.

Zhong, Q., D. Inniss, K. Kjoller, and V. B. Elings. 1993. Fractured polymer silica fiber surface studied by tapping mode atomic-force microscopy. *Surface Sci.* 290:L688–L692.